Pulsed-laser-induced dewetting in nanoscopic metal films: Theory and experiments

Justin Trice,[1,2] Dennis Thomas,[3] Christopher Favazza,[1,2] Radhakrishna Sureshkumar,[2,3,*] and Ramki Kalyanaraman[1,2,†]

[1]*Department of Physics, Washington University in St. Louis, Missouri 63130, USA*
[2]*Center for Materials Innovation, Washington University in St. Louis, Missouri 63130, USA*
[3]*Department of Energy, Environmental and Chemical Engineering, Washington University in St. Louis, Missouri 63130, USA*
(Received 8 September 2006; revised manuscript received 9 April 2007; published 22 June 2007)

Hydrodynamic pattern formation (PF) and dewetting resulting from pulsed-laser-induced melting of nanoscopic metal films have been used to create spatially ordered metal nanoparticle arrays with monomodal size distribution on SiO_2/Si substrates. PF was investigated for film thickness $h \leq 7$ nm$<$laser absorption depth ~ 11 nm, and different sets of laser parameters, including energy density E and the irradiation time, as measured by the number of pulses n. PF was only observed to occur for $E \geq E_m$, where E_m denotes the h-dependent threshold energy required to melt the film. *Even at such small length scales*, theoretical predictions for E_m obtained from a continuum-level lumped parameter heat transfer model for the film temperature, coupled with the one-dimensional transient heat equation for the substrate phase, were consistent with experimental observations provided that the thickness dependence of the reflectivity of the metal-substrate bilayer was incorporated into the analysis. The model also predicted that perturbations in h would result in intrinsic thermal gradients $\partial T/\partial h$ whose magnitude and sign depend on h, with $\partial T/\partial h > 0$ for $h < h_c$ and $\partial T/\partial h < 0$ for $h > h_c \approx 9$ nm. For the thickness range investigated here, the resulting thermocapillary effect was minimal since the thermal diffusion time τ_H is less than or equal to the pulse time. Consequently, the spacing between the nanoparticles and the particle diameter were found to increase as h^2 and $h^{5/3}$, respectively, which is consistent with the predictions of the thin-film hydrodynamic (TFH) dewetting theory. PF was characterized by the appearance of discrete holes followed by bicontinuous or cellular patterns which finally consolidated into nanoparticles via capillary flow rather than via Rayleigh-like instabilities reported for low-temperature dewetting of viscous liquids. This difference is attributed to the high capillary velocities of the liquid metal arising from its relatively large interfacial tension and low viscosity as well as the smaller length scales of the liquid bridges in the experiments. The predicted liquid-phase lifetime τ_L was between 2 and 15 ns, which is much smaller than the dewetting time $\tau_D \geq 25$ ns as predicted by the linear TFH theory. Therefore, dewetting required the application of multiple pulses. During the early stages of dewetting, the ripening rate, as measured by the rate of change of characteristic ordering length with respect to n, increased linearly with E due to the linear increase in τ_L with increasing E as predicted by the thermal model. The final nanoparticle spacing was robust, independent of E and n, and only dependent on h due to the relatively weak temperature dependence of the thermophysical properties of the metal (Co). These results suggest that fast thermal processing combined with the unique thermophysical parameters of metals can lead to a different pattern formation, including quenching of a wide range of length scales and morphologies.

I. INTRODUCTION

Physical phenomena that impose patterns with characteristic length scales can be utilized for the self-assembly of spatially ordered metal nanoparticles which have various applications, including magnetics, catalysis, nanophotonics, and plasmonics.[1–7] Nonlinear dynamical instabilities which evolve into a robust stable state characterized by a narrow range of length scales are especially well suited for this purpose. Typically, such self-assembly of ordered patterns on surfaces and thin films arises from the competition between various physicochemical effects. For example, surface rippling under ion irradiation can be attributed to an instability resulting from the competition between irradiation-induced ion erosion and smoothing due to surface diffusion. The length and time scales of the ensuing patterns are determined by ion flux, surface temperature, and surface diffusion parameters.[8–14] Alternately, nanopatterns could result from instabilities of a thin fluid layer leading to spatiotemporal reorganization of the fluid with well-defined length and time

scales that depend on the thermophysical material properties such as interfacial tension, fluid/substrate contact angle, fluid viscosity, and, for ultrathin films, long-range dispersion forces such as van der Waal's interactions. An example of pattern formation by such instabilities is dewetting of thin films caused by a hydrodynamic instability which occurs when attractive intermolecular forces overcome the stabilizing effect of interfacial tension.[15–18] Under such conditions, film thickness fluctuations are spontaneously amplified eventually leading to film rupture and the formation of drops and/or particles with well-defined spatial order.[19]

Dewetting dynamics leading to particle formation have been studied in detail in polymer films that are in the liquid state close to room temperature.[20–23] In comparison, studying dewetting in metals is challenging due to the high melting point of most metals. Metal dewetting under conventional long-time annealing is complicated because various surface processes including metal-substrate chemical interactions and metal diffusion into the substrate can influence dewetting.[24,25] On the other hand, rapid melting techniques

such as ion irradiation[26,27] or nanosecond pulse laser heating could minimize such undesirable effects and permit experiments over practical time scales.[28,29] Approximately ten years ago, it was shown that 1 ns laser-pulse melting of various metals (Au, Cu, and Ni) on a Cr *metal layer* resulted in dewetting patterns with spatial order.[30,31] However, pattern formation and self-assembly of spatially ordered patterns under pulsed-laser dewetting of metal films deposited directly on SiO$_2$ (a substrate of choice for many optoelectronic applications) have not been pursued in great detail, especially in nanoscopic metal films with thickness h less than the laser absorption depth α_m^{-1}. Furthermore, pattern evolution under the application of thermally independent multiple pulses (i.e., the film undergoes melting during the pulse and resolidification between pulses), with varying laser parameters to understand the dynamics of metal dewetting, as well as the length scales of a variety of different patterns have not been investigated. This is of fundamental importance since the *unique* thermophysical properties of metallic liquids, including their high surface tension γ of $O(1)$ J/m^2 and large thermal conductivities, distinguish them from the typical liquid polymers $[\gamma \sim O(10^{-2})$ J/m$^2]$ investigated in the past. Therefore, liquid metals could present novel patterning mechanisms and/or characteristics. Another important question of broader fundamental interest is related to the applicability of *continuum-level* conservation equations (for heat, mass, and momentum) at the nanoscopic length scales ($h < \alpha_m^{-1}$ ~ 11 nm) used in the present experiments. Note that the application of atomistic or mesoscopic techniques to problems which involve phase change and surface deformation under fast thermal cycles is not entirely straightforward and first-principles-based atomistic and/or mesoscopic simulations of such phenomena are beyond present capabilities. Hence, the importance of developing experimentally validated continuum-level models for such processes cannot be over-emphasized.

Recently, we showed that multiple nanosecond pulsed-laser melting of nanoscopic Co films leads to short- and/or long-range spatial order.[32–34] We provided preliminary evidence that dewetting by multiple nanosecond pulse-laser melting shows characteristics of a thin-film hydrodynamic (TFH) instability, such as the spinodal process.[32] This was based on the observation that the final nanoparticle morphology, quantitatively described by the nearest-neighbor (NN) particle spacing (R) and diameter (D), is consistent with the prediction of the linear TFH theory which was modified to incorporate long-range intermolecular attractive forces of van der Waal's type. However, the quantitative role of various laser parameters including the energy density E and time (as measured implicitly by the number of pulses n) on pattern evolution was not investigated in detail. In this work, we present a detailed account of pattern formation and dewetting under *multiple* nanosecond pulsed-laser irradiation of Co nanofilms ($h \lesssim 7$ nm and $\alpha_m^{-1} \sim 11$ nm) on SiO$_2$ in the light of first-principles thermal modeling and TFH theory (Sec. III) and discuss other physical mechanisms specific to dewetting of nanolayers of liquid metals.

The remainder of the paper is organized as follows. In Sec. II, the experiment and modeling details are presented. In

Sec. III A, we show that by accounting appropriately for the changes in the reflectivity of the substrate-metal bilayer with respect to h, quantitative agreement can be obtained between experimental observations and the predictions of continuum-level theory for the h dependence of the melting energy threshold, pattern length scale, and particle size. This observation corroborates atomistic simulations of heat transport for simpler fluids under shear flow which, for liquid layers with several (six to seven) atomic layers,[35] yielded thermal profiles consistent with predictions of continuum-level analysis. For the metal films used in this work, this translates to $h = 1$ nm. The thermal model also predicted the development of intrinsic thermal gradients $\partial T / \partial h$, whose sign is positive for h less than a critical value $h_c \approx 9–13$ nm and negative for $h > h_c$. This would imply that thermocapillary effects (i.e., flow induced by surface-tension gradient along the perturbed interface which samples an h-dependent temperature field) could also be an important mechanism of pattern formation. For the experimental thickness regime investigated, the thermal diffusion time scales τ_H is less than or equal to the pulse time $t_p = 9$ ns and therefore the influence of $\partial T / \partial h$ were observed to be minimal. However, since $\tau_H \propto h^4$, thermocapillary mechanisms could be important for thicker films, a hypothesis that needs to be verified by future experimental studies. In Sec. III B, we discuss the quantitative behavior of pattern evolution as a function of E and n. Extremely fast thermal cycles [heating and/or cooling rates of $O(10^{10}$ K/s)] were predicted by the thermal modeling, implying that each laser pulse was thermally independent of one another (repetition rate: 50 Hz). Furthermore, the model predicted liquid lifetimes τ_L of $2–15$ ns, while the linear TFH theory[15] predicted a dewetting time scale $\tau_D \gtrsim 25$ ns, implying that multiple pulses would be required to observe the instability, as confirmed by experiments. We suggest that once dewetting was initiated by melting of the thin film, subsequent pulses continued to foster the instability and each laser pulse captured snapshots of its progression. Experimentally, the dewetting patterns were characterized by short-range order (SRO) at all observed stages of dewetting, with the patterns typically evolving with increasing number of laser pulses n from discrete holes to bicontinuous or cellular structures and eventually into nanoparticles. These nanoparticles form by capillary flow rather than a Rayleigh-like breakup typically observed in polymer liquids. This behavior can be attributed to the large capillary velocity (ratio of interfacial tension γ to fluid viscosity η) for the metal nanolayers resulting from its unique thermophysical parameters, including a large $\gamma = 1.88$ J/m^2, small $\eta = 4.45 \times 10^{-3}$ Pa s, and small pattern length scales due to its large Hamaker constant $A \sim 10^{-18}$ J. This final nanoparticle state was robust, characterized by SRO in NN spacing R and a monomodal size distribution with diameter D with the observed trends of $R \sim h^2$ and $D \sim h^{5/3}$, respectively. This robustness could be explained by two effects: (i) the relatively weak temperature dependence of the thermophysical parameters of Co and (ii) the minimal particle coarsening due to surface diffusion, since the diffusion time scale is much greater than that of the thermal processing time t_p. In Sec. III C, we show that the pattern ripening rate L/n, where L is the characteristic pattern length, increased linearly with E at the early stages of

patterning, which could be explained by the predicted linear increase in τ_L with E. Overall, these results show that pattern formation and dewetting in liquid metal nanolayers under fast thermal cycles can result in other mechanisms and, experimental observations in conjunction with theoretical analyses of thermal cycles and TFH instabilities offer quantitative guidelines for achieving desired quenched-in morphologies with predictable length scales.

II. PULSED-LASER PROCESSING: EXPERIMENT AND THERMAL MODELING

A. Experimental details

Cobalt metal films with thickness in the range $1 \leq h \leq 7$ nm were deposited at the rate of 1 nm/min onto optical quality SiO_2/Si substrates at room temperature. The substrates were commercially obtained with a 400-nm-thick thermally grown oxide layer on polished Si(100) wafers. Deposition was done under vacuum conditions (2×10^{-8} Torr) by electron-beam evaporation from a TECTRA e^--flux mini electron-beam evaporator. The wafers were degreased in acetone, methanol, and de-ionized water prior to film deposition. The film thickness was controlled through the deposition rate as measured using an *in situ* Inficon XTM/2 deposition monitor. The final thickness was established by calibrating concentration measurements of Co film using energy dispersive x-ray spectrometry (EDS) in a scanning electron microscope (SEM) to measurements by Rutherford backscattering.[36,37] During each deposition run, up to eight pieces of the substrate measuring approximately 5×5 mm^2 were placed such that a number of different irradiation experiments could be performed in vacuum. The thickness variation between the different pieces in a single run was measured to be less that 10%. For every film thickness we also made atomic force measurements (AFM) of the surface roughness and an upper limit of 0.1 ± 0.03 nm was established for the average rms roughness over the entire film thickness range. AFM was performed in ambient conditions using a Molecular Imaging PicoScan AFM with a tip of spring constant 0.2 N/m. The measured lateral ($x-y$) resolution was ~ 10 nm and z-height resolution was ~ 0.2 nm. A Hitachi S-4500 field-emission microscope operating at 15 kV was used for EDS and SEM measurements. The spatial resolution of this microscope was ~ 1.5 nm.

The films were irradiated in vacuum at normal incidence by a laser beam of variable beam size controlled by a 500 mm biconvex lens, with a maximum size of 3×3 mm^2. The laser used was a Spectra Physics Injection seeded Lab-130-50 Nd:YAG (yttrium aluminum garnet) laser operating at its fourth harmonic with wavelength $\lambda = 266$ nm at 50 Hz repetition rate. Based on the thermal model (Sec. III B), the metal film is expected to return to room temperature within approximately 500 ns and therefore each laser pulse could be viewed as being thermally independent of one another. The laser beam was plane polarized with a coherence length of ~ 2 m and had a Gaussian temporal shape. The pulse width t_p, as measured by the full width at half maxima of the temporal profile, was 9 ns. The spatial profile of the beam was a circular multimode energy distribution established by the dif-

fraction output coupler of this laser. The spatial energy distribution was best described by fitting to a Gaussian shape which gave an 85% fit to the centroid of the distribution in each direction with a full width at half maxima of 4 mm. In the studies reported here, all morphology investigations were reported from approximately 50×100 μm^2 region of the irradiated area within which the laser energy density variation was less than or equal to 10% in each of the two dimensions.

Two types of laser irradiation experiments were performed. The first was a determination of the melt threshold laser energy density, E_m. We defined E_m as the minimum energy density at which a morphology change could be detected after the shortest irradiation time of ten laser pulses. We also verified that for $E < E_m$, no morphology change could be observed even after the longest irradiation time of 10 500 pulses, thus ruling out contributions from surface diffusion. The morphology change observed was a typical dewetting pattern observed in the SEM, as shown in Sec. III B. Such an approach has been successfully used in the past to detect melt threshold of thin films under laser irradiation.[38] The laser energy density was controlled by varying the lens-sample position and/or the laser energy, which was measured using an Ophir Electronics PE30 A-P high-power laser detector head with an Orion power meter. In this manner, energy densities ranging from 10 from 1000 mJ/cm^2 can be achieved. The second study was of dewetting pattern evolution as a function of various energy densities $E \geq E_m$ and over a range of irradiation times, as measured by the number of pulses n. The irradiation time is typically in the range $10 \leq n \leq 10\,500$. The pulse number was controlled by a shutter in the beam path. Each independent irradiation, i.e., with a different E and/or n, was performed on different pieces of the substrate and each was characterized using SEM and/or AFM measurements. While the lower limit on the choice of E was set by E_m, the upper limit was set by ensuring that after the longest irradiation times no substantial evaporation ($\leq 15\%$) had occurred. This was ensured by measuring the concentration of the metal after irradiation via EDS in the SEM and by comparing with the thickness calibrated values. In this manner, detailed information on pattern formation was obtained as a function of E and n for each h under conditions not influenced by evaporation.

B. Thermal transport modeling

Given the applicability of continuum-level modeling established in this work, we point out that the nanoscopic length scales allow certain simplifications, which in turn allowed obtaining insightful analytical solutions for the film temperature as a function of time. The simplifications include (i) $h < \alpha_m^{-1}$ and (ii) the heat loss occurring primarily through conduction through the substrate. Typically for pulse durations > 1 ns, Fourier heating theory is found to be applicable and, consequently, the laser heating may be modeled by a position-dependent source term in the transient energy equation.[39] The heat transport model was developed to simulate the experiment of heating by a pulsed-laser beam incident normal to the film-substrate bilayer with a spatially uniform energy profile in the plane ($x-y$) of the bilayer that was

infinitely wide in the *x* and *y* directions. For these conditions, the relevant heat diffusion was normal to the film surface in the *z* direction, where $z = -h$ corresponds to the vacuum-film interface and $z = 0$ the film-substrate interface. The following assumptions were made in formulating the heat transfer problem: (1) The substrate layer was viewed as a semi-infinite medium ($0 \leq z < \infty$). In the case of SiO$_2$ for UV irradiation, the substrate served strictly as a conducting medium since it was transparent to UV. (2) The thermal contact resistance at the film-substrate interface was neglected, which is justified *a posteriori* as follows. The numerically predicted thermal flux at the film-substrate interface is of order $\sim 10^{10}$ W/m^2 for films irradiated with laser energy densities in this work ranging from ~ 50–350 mJ/cm^2. Typical values of thermal resistance for thin films range from 10^{-5} to 10^{-11} K m^2/W,[40] implying that an addition of thermal impedance would lead to model predictions for the melting threshold which are significantly lower than its experimentally measured values.

In the above framework, the film temperature $T^*(z,t)$ is described by

$$(\rho C_{eff})_m \frac{\partial T^*}{\partial t} = k_m \frac{\partial^2 T^*}{\partial z^2} + S^* f(t) \alpha_m \exp[-\alpha_m(z+h)], \quad (1)$$

where the subscripts *m* and *s* denote the metal and substrate, respectively, ρ is the density, C_{eff} is the effective heat capacity, S^* is the rate of energy flux absorbed from the laser into the film, $f(t)$ denotes the temporal energy distribution of the laser source, and α_m is the absorptivity of the metal film at 266 nm. Specifically, $f(t) = 1$, $1 - H(t - t_p)$, and $e^{-(t-t_p)^2/2\sigma^2}$ for uniform, square-shaped, and Gaussian pulses, respectively, with *H* denoting the Heaviside step function. We are interested in the average film temperature, especially since the spatial variations in T^* are expected to be small since $h < \alpha_m^{-1}$ and thermal diffusion time scale $< t_p$. An equation for $T \equiv \frac{1}{h}\int_{-h}^0 T^* dz$ can be obtained by integrating Eq. (1) with respect to *z* from $z = -h$ to $z = 0$ and dividing throughout by *h*:

$$(\rho C_{eff})_m \frac{dT}{dt} = -\frac{q_s}{h} + \frac{S^* f(t)}{h}[1 - \exp(-\alpha_m h)], \quad (2)$$

where $q_s(t) \equiv -k_m(\partial T^*/\partial z)_0 = -k_s(\partial T_s/\partial z)_0$ is the conductive heat transfer to the substrate, where T_s denotes the substrate temperature field. Note that the radiative heat transfer from the film surface to the vacuum is typically much smaller than the conductive transport to the substrate. Hence, $(\partial T^*/\partial z)_{z=-h}$ is set to 0. Thus, the lumped parameter equation is valid for all *h* given that *T* is interpreted as the average temperature in the film. Evidently, for $h < \alpha_m^{-1}$, the gradients would be sufficiently small so that this would be a good approximation to the uniform film temperature. Letting $S = \frac{S^*[1 - \exp(-\alpha_m h)]}{(\rho C_{eff})_m h}$, the time-dependent temperature in the metallic monolayer can be expressed as

$$\frac{dT}{dt} = Sf(t) - \frac{q_s(t)}{(\rho C_{eff})_m h}, \quad (3)$$

where *S* is the rate of energy absorbed from the laser, averaged over the film. For a Gaussian-shaped pulse, we have

$$S^* = [1 - R(h)]\frac{E_o}{\sqrt{2\pi}\sigma}, \quad (4)$$

and for constant heating or a square pulse,

$$S^* = [1 - R(h)]\zeta\frac{E_o}{t_p}, \quad (5)$$

where *R* is the *h*-dependent reflectivity for the laser at normal incidence. The general expression for the effective *R* value for an absorbing film on a transparent substrate has been derived previously[41] and for Co-SiO$_2$, over the film thickness range of interest, it is well represented by a saturating exponential of type $r_o(1 - e^{-a_r h})$, with $r_o = 0.44$ and $a_r^{-1} \sim 15.5$ nm. Further, in the above expressions, E_o is the laser energy density, σ is the standard deviation chosen so that the length of the Gaussian full width at half maximum is equal to the laser pulse width t_p, and ζ is a renormalization factor to ensure that the total energy absorbed per pulse is identical for the square and Gaussian models. The temperature field in the substrate was described by the variable $\Theta_s \equiv T_s - T_0$, where $T_0 = T_s(z \rightarrow \infty)$:

$$\frac{\partial \Theta_s}{\partial t} = a_s \frac{\partial^2 \Theta_s}{\partial z^2}, \quad (6)$$

where the substrate thermal diffusivity $a_s = \frac{k_s}{(\rho C_{eff})_s}$, with initial and boundary conditions $\Theta(z,0) = \Theta(\infty,t) = 0$ and $-k_s\frac{d\Theta}{dz}(0,t) = q_s(t)$, which couples the substrate and film temperature fields. By employing the method of Laplace's transforms, the above set of equations can be solved to yield

$$T(t) = T_o + \frac{2}{\sqrt{\pi}}\left(\frac{S}{K}\right)\sqrt{t} + \frac{S}{K^2}[e^{K^2 t}\,\mathrm{erfc}(K\sqrt{t}) - 1]$$
$$- S\int_0^t e^{K^2(t-u)}\,\mathrm{erfc}(K\sqrt{t-u})H(u-t_p)du, \quad (7)$$

where $K = \frac{\sqrt{(\rho C_{eff}k)_s}}{(\rho C_{eff})_m h}$, and the integral in Eq. (7) may be solved numerically. Now, for the case of the Gaussian model, the solution for $T(t)$ is given by

$$T(t) = T_o + S'\int_0^t \exp(-f^2(t-u)^2 + g(t-u)$$
$$+ K^2 u)\mathrm{erfc}(K\sqrt{u})du, \quad (8)$$

where $f = 1/\sqrt{2}\sigma$, $g = 2t_p f$, and $S' = S\exp(-f^2 t_p^2)$. The integral in Eq. (8) may be solved numerically using standard software packages. For both the Gaussian and square pulse solutions, we used the Riemann midpoint rule to evaluate the integral with MAPLE™ v9.1. We note that for a uniform pulse [$f(t) = 1$], a simpler analytical solution of the following form can be obtained:
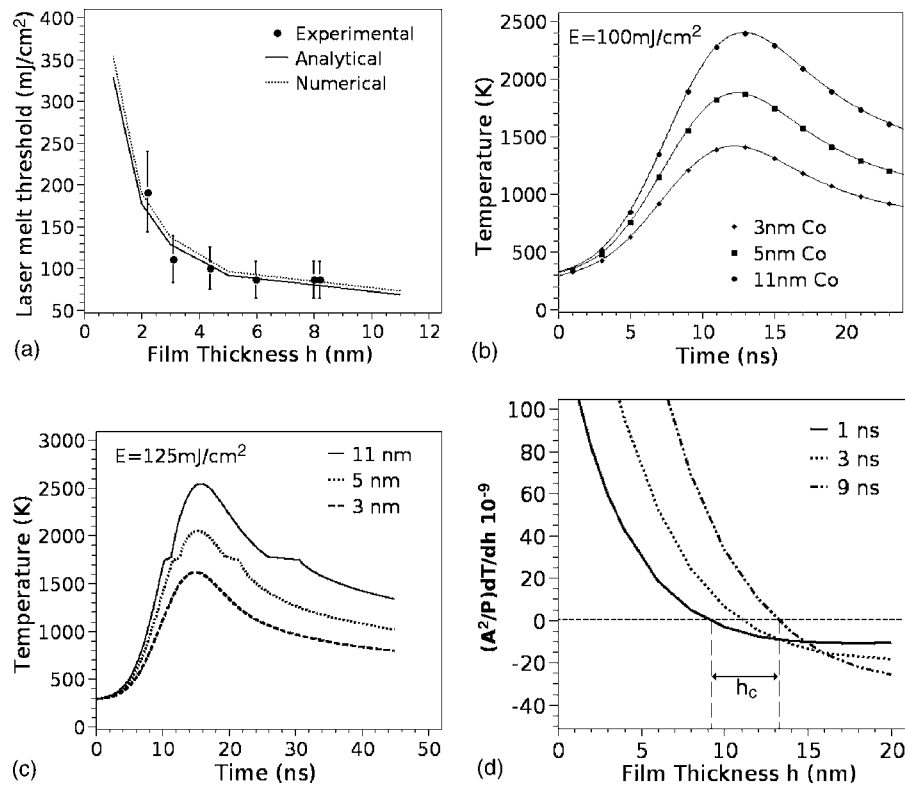
FIG. 1. Thermal behavior of the Co film on SiO_2 irradiated by a pulsed laser. (a) Laser energy density threshold for melting E_m of Co films on SiO_2. Comparison of experimental measurement (solid circles) with calculations from our analytical model (solid line) and numerical model (dashed line). (b) Time-dependent temperature obtained for the analytical and numerical models using temperature-independent parameters. The symbols are from the analytical model, while the lines are from the numerical calculations. (c) Numerical results incorporating the phase change and T-dependent parameters for various film thicknesses. (d) Intrinsic thermal gradient $\partial T/\partial h$ predicted from the thermal model whose magnitude and sign were dependent on film thickness and time to melt during the ultrafast heating of nanoscopic metal films. For the thickness regime investigated in this work ($h \leqslant 7$ nm), the $\partial T/\partial h$ dissipates in $t < t_p$ and this intrinsic effect is negligible.

$$T(t) = T_o + \frac{2}{\sqrt{\pi}}\left(\frac{S}{K}\right)\sqrt{t} + \frac{S}{K^2}[e^{K^2 t}\,\mathrm{erfc}(K\sqrt{t}) - 1], \quad (9)$$

which for $t > 1/K^2$ (where $1/K^2$ ranges from 4.8×10^{-3} to 5.9×10^{-1} ns corresponding to Co film thickness of $1-11$ nm) would predict a temperature rise proportional to $\sqrt{t}$. While this solution is insightful, it overpredicts the temperature rise within the film. Hence, a more realistic Gaussian temporal distribution has been employed in the subsequent analysis.

In order to validate the assumptions made in the analytical treatment, a two-phase transient heat transfer model was also solved numerically using the finite-element method by using the commercial software FEMLAB™ v3.1. Here, the assumption of homogeneous temperature in the film was relaxed. In order to mimic the semi-infinite substrate phase, the boundary condition $T_s (z,t)|_{z=5L_{th}} = T_o$ was imposed, where L_{th} is the thermal diffusion length of the substrate $\approx \sqrt{t_p a_s}$ where a_s is the thermal diffusivity of the substrate. The simulations were performed for different spatial and temporal resolutions to ensure numerical convergence. For temperature-independent thermophysical parameters, we observed good agreement between the analytical and numerical results for T within 0.5 K

[see Fig. 1]. First-order phase transition was modeled by using an effective heat-capacity technique based on previous approaches,[42,43] namely, $C_{eff} = C_p + L\frac{\partial F}{\partial T}$, where

$$F(T) = \begin{cases} \dfrac{T}{2\varepsilon} & \text{for } T_m - \varepsilon < T < T_m + \varepsilon \\ 0 & \text{otherwise}, \end{cases}$$

L is the latent heat of transformation for the film, and T_m is the melting temperature of the film. The functional form of $F(T)$ was chosen so that C_{eff} models a first-order phase change; i.e., when $\frac{\partial F}{\partial T}$ is integrated from $T_m - \varepsilon$ to $T_m + \varepsilon$, the result equals unity. Here, ε is a small temperature parameter whose value was chosen so that no oscillation in T would be observed during the melting and freezing transitions. A value of $\varepsilon = 15$ K was sufficient to ensure oscillation-free results in the simulations reported here. The temperature-dependent and -independent material parameters are tabulated in Table I. All simulations predicted the maximum temperature difference between the film-surface and film-substrate interfaces to be $\ll 1$ K. This indicated that the z-averaged temperature field obtained from the analytical model can be interpreted as a nearly uniform film temperature.

TABLE I. Material and scaling parameters (T dependent and T independent) used in modeling.

Quantity	Description	Value/Expression	Reference
$\sigma = t_p/2\sqrt{2\ln(2)}$	Standard deviation	3.822 ns	
$R(h)$	Thickness-dependent reflectivity	$R_{\mathrm{SiO_2}} \leqslant R \leqslant R_{\mathrm{Co}}$	41 and 44
α_m^{-1}	Absorptivity	9.21×10^7 cm^{-1}	44
L	Heat of transformation	274 J/g for Co	51
T_m	Melting temperature	1768 K for Co	51
ρ_m	Metal film density	$[8.9[1-H(T-T_m)]+7.75H(T-T_m)]$g/cm^3	51
ρ_s	Substrate density	2.2 g/cm^3	52
$[C_{eff}(T)]_m$	Temperature-dependent film heat capacity	$[0.42[H(T)-H(T-T_m)]+0.59H(T-T_m)]$J/g K	51
$(C_{eff})_m$	Temperature-independent film heat capacity	0.42 J/g K	51
$[C_{eff}(T)]_s$	Temperature-dependent substrate heat capacity	$[0.931+(2.56\times10^{-4})T-0.240/T^2]$J/g K	52
$[C_{eff}]_s$	Temperature-independent substrate heat capacity	0.937 J/g K	52
$k_m(T)$	Temperature-dependent film thermal conductivity	$(0.0912+264.65/T)[H(T)-H(T-1000)]+(-0.0016T$ $+2.4402)[H(T-1000)-H(T-1400)]$W/cm K	53 and 54
k_m	Temperature-independent film thermal conductivity	1 W/cm K	51
k_s	Substrate thermal conductivity	0.014 W/cm K	52
ζ	Scaling constant	0.76	
ϵ	Phase change tuning parameter	15 K	
T_o	Room temperature	300 K	
$\gamma(T=T_{mp})$	Surface tension	1.88 J m^{-2}	
γ_T	$d\gamma/dT$	-0.5×10^{-3} J m^{-2} K^{-1}	
$\eta(T)$	Viscosity	$0.3272\times10^{-3}e^{(0.3742\times10^5/RT)}$ Pa s	
η_T	$d\eta/dT$	$(-4500.8/T^2)\eta(T)$Pa s K^{-1}	

III. RESULTS AND DISCUSSION

A. Laser energy threshold E_m to observe dewetting versus thickness

1. Experiment

The morphology of the films was first investigated as a function of increasing laser energy density over a practical time scale ranging from a few laser pulses to a maximum of 10 500 laser pulses. The first observation was that below a critical E no perceptible morphology change could be observed even after the longest irradiation. On the other hand, above this energy, significant morphology changes could be observed even after the shortest irradiation time ($n=10$). This sharp threshold behavior implied that a phase-change process, such as melting, rather than surface diffusion was responsible for the morphology change. Using this approach, a measurable critical E was obtained for a range of film thickness. The experimentally determined behavior of E_m vs h is plotted in Fig. 1(a) (filled circles). This observed trend, i.e., a significant increase in E_m with decreasing h for the ultrathin films ($h \leqslant 5$ nm), is consistent with the prediction of Ref. 38 and the underlying mechanisms that contribute to this behavior are discussed below.

2. Modeling

In order to determine whether the energy E_m is closely correlated to the melt threshold, we used the analytical and numerical models to estimate the melt threshold energy. This

was obtained by simulating the thermal behavior under the pulse for various energies. Figure 1(b) shows a plot of Eq. (8) versus time for various Co film thicknesses h with a laser energy density value of $E=100$ mJ/cm^2 estimated using the analytical model. The points represent Eq. (8) solved at various times and the lines represent the corresponding finite-element simulations. Predictions of a numerical simulation incorporating phase change and temperature-dependent material parameters are shown in Fig. 1(c). In addition, from Eq. (8), the melt threshold energy E_m, which is the value of E needed to bring the Co film to melting temperature, was calculated. The time t_m, where Eq. (8) reaches its maximum temperature, was first determined for various film thicknesses. Then, Eq. (8) was set equal to T_m at $t=t_m$ and solved for the appropriate value of E by successive approximations. Analytical predictions for the melt threshold energy versus h are shown in Fig. 1(a) as the solid line along with the numerically predicted laser melt threshold energy density (dashed line). From Fig. 1(a), an increasing E_m with decreasing h is obtained for experiment and modeling, and furthermore, the estimated E_m is in excellent agreement with experiment. Based on this result, we interpreted the experimentally measured E_m to be the melt threshold energy, and all dewetting behavior was investigated for energies at or above the E_m for the various h.

Equation (9) can be used to explain the intriguing thermal behavior. Specifically, the temperature rise is proportional to $S/K \propto f_1(h)f_2(h)$, where $f_1(h) \equiv 1-\exp(-\alpha_m h)$ and $f_2(h) \equiv 1-r_0+r_0\exp(-a_r h)$ represent the contributions to the source

term [S in Eq. (3)] from finite laser absorption depth of the metal and metal/substrate bilayer reflectivity, respectively. It is easily verified that f_1 increases while f_2 decreases with increasing h. However, since $\alpha_m > a_r$, the net effect is an increase in S/K with increasing h. Consequently, thicker films will experience faster heating rates. However, note that if one disregards the latter effect (of reflectivity), the model would overpredict the temperature rise by approximately 6% and 26% for $h=2$ and 10 nm, respectively. This suggests that appropriately accounting for the thickness dependence of the reflectivity is important to arrive at predictions which are quantitatively consistent with experimental measurements. Moreover, the sensitivity of S/K to laser-metal interaction parameters implies that the thermal behavior and hence the pattern formation itself could be highly system dependent. With the thickness-dependent reflectivity of the metal-substrate bilayer varied from the value for bulk SiO_2 of $R \sim 0$ for $h_m=0$ to the value for bulk Co of $R=0.44$ (Ref. 44) and in the thickness regime of interest in this work, i.e., $h_m \leq \alpha_m^{-1}$, the calculated value is significantly smaller than that for bulk Co.

Another important result obtained from the thermal modeling is the prediction of an intrinsic thermal gradient $\partial T/\partial h$ that can result in temperature variations along the film whenever the irradiated film has height fluctuations, i.e., employing a local approximation, $\partial T/\partial x = (\partial T/\partial h)\partial h/\partial x$. The length scale of the interface height fluctuations (or the interface roughness) $\sim \sqrt{k_B T/\gamma} \approx 0.2$ nm for a liquid Co film at 1700 K. While such perturbations are randomly distributed, TFH theory predicts that a wavelength with fastest growing time scale (or eigenvalue, see Sec. III B 3 below) will be preferentially amplified and become the dominant, observable length scale. Temperature variations could result in surface tension gradients along the interface, which in turn will induce thermocapillary flow that can reduce ($\partial T/\partial h > 0$) or enhance ($\partial T/\partial h < 0$) the dewetting rate via thermocapillary flows that promote fluid motion from the crest (trough) to the trough (crest) of the perturbed interface. Specifically, $\partial T/\partial h$ can be estimated from Eq. (9) and the resulting dependence on h is shown in Fig. 1(d), where the ordinate $\frac{\partial T}{\partial h}$ is scaled by the numerical factor $(A^2/P)10^{-9}$, where $A = \frac{\sqrt{(\rho C_{eff} k)_s}}{(\rho C_{eff})_m}$ and $P = \frac{\zeta E_o}{(\rho C)_m t_p}$ are material- and laser-related parameters. As seen from Fig. 1(d), the rate of change in temperature, evaluated for different times to melt of the films, is a strong function of film thickness. One can clearly note that $\partial T(t,h)/\partial h$ becomes negative at a certain critical thickness h_c when the film melts over reasonable time scales. h_c is observed to lie between ~ 9 and 13 nm, corresponding to melting times between 1 and 9 ns. The time scale over which $\partial T/\partial h$ will be effective is the thermal diffusion time scale τ_H in the Co metal films, and this time should be compared to pulse time t_p. Clearly, if $\tau_H/t_p \leq 1$, then thermal diffusion would smooth out $\partial T/\partial h$ effects over the time of heating and its role on pattern formation would be negligible. As we will show in Sec. III B 3, the metal dewetting is most likely due to a TFH hydrodynamic instability similar to spinodal dewetting. According to this model, the dewetting length scale Λ varies as h^2 and thus the relevant thermal diffusion time is $\tau_H \propto \Lambda^2/D_{th}^{Co} \propto h^4$,

where $D_{th}^{Co}=2.7 \times 10^{-5}$ m^2/s is the thermal diffusivity of Co. Using the quantitative expression for Λ obtained in Sec. III B 3, we determined that up to thickness of $h \sim 6$ nm, $\tau_H \leq t_p$ and therefore the intrinsic thermocapillary effects will only have a minimal influence of pattern formation for the thickness regime investigated here, $1 \leq h \leq 7$ nm. On the other hand, since $\tau_H \propto h^2$, significant modifications to pattern formation for thick films is likely, including changes to patterning length and time scales. However, a detailed investigation for thickness above 7 nm is beyond the scope of the present work.

B. Dewetting pattern evolution with n and E

A detailed investigation of the dewetting morphology was performed for various laser energies as a function of the laser irradiation time n. For films in the range of $3 \leq h \leq 7$ nm, the patterns typically consisted of discrete holes at the early stages of irradiation, followed by cellular patterns at later stages, and eventually, nanoparticles which remained stable to irradiation. On the other hand, for the films with $h < 3$ nm, the morphology consisted of discrete holes followed by a bicontinuous structure with a final state again characterized by nanoparticles. It is widely accepted that the dewetting morphology can arise from three mechanisms:[45] (i) homogeneous nucleation and growth in which holes appear randomly in location and time on the surface, therefore, no characteristic length is present in this type of dewetting;[22] (ii) heterogeneous nucleation and growth due to defects, impurities, or other experimentally imposed heterogeneities (here, a characteristic length scale could appear at the early stages of dewetting due to ordered nucleation sites; for instance, in ion-irradiation-induced dewetting, the average molten zone of an ion imposes a characteristic length scale in dewetting[27]); and (iii) TFH instabilities such as the one associated with the dewetting of spinodally unstable systems. The resulting patterns were characterized by a well-defined length scale in the hole spacing and/or size.[21] Since we have ruled out spatially ordered heterogeneities on the surface and in the film microstructure, the results presented below were analyzed to distinguish between dewetting by homogeneous nucleation and TFH instabilities that establish a characteristic length scale. In order to do this, the primary characterization was the evaluation of the patterning length scales obtained from the power spectrum (PS) evaluated by performing fast Fourier transforms of the morphology of the dewetting patterns.

1. Dewetting morphology for $h < 3$ nm

Figures 2(a)–2(d) capture the morphology of a 2-nm-thick Co film as a function of increasing number of laser pulses at energy 200 mJ/cm^2. Discrete holes were visible after the shortest time [Fig. 2(a)], with the patterns changing to a bicontinuous structure [Figs. 2(c) and 2(d)] and finally into nanoparticles [Fig. 2(d)]. A comparison of the density of features in Figs. 2(c) and 2(d) indicates that the nanoparticles form by changing spaghettilike features into a single particle
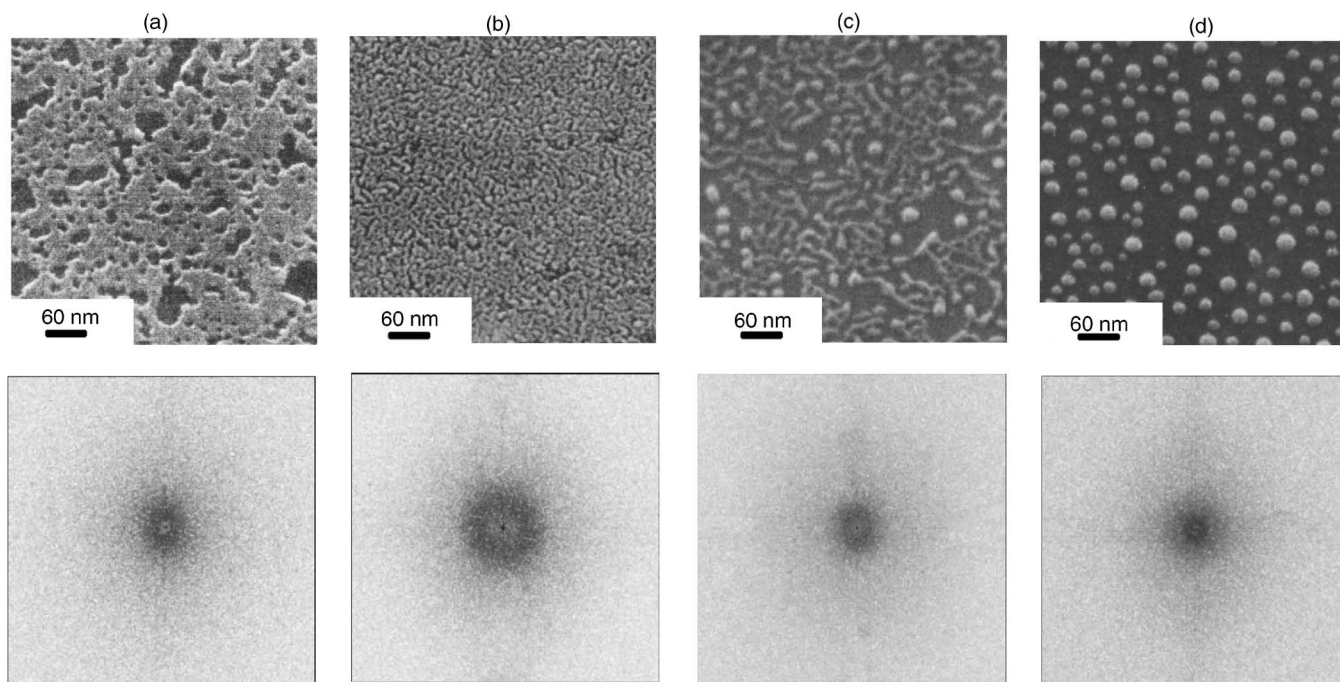
FIG. 2. Dewetting pattern evolution in a 2 nm Co film irradiated at 200 mJ/cm^2 as a function of number of pulses n. The top row are SEM images, while the bottom row show corresponding power spectrum: (a) $n=10$, (b) $n=100$, (c) $n=1000$, and (d) $n=10\,500$. All the power spectra have an annular structure, indicating a band of spatial frequencies and implying short-range spatial order.

rather than break up of the spaghettilike features into multiple particles, such as in a Rayleigh-like process. As shown in Fig. 5(a), the nanoparticles had a monomodal size distribution. The spatial behavior of the patterns could be understood from the PS, as shown in Figs. 2(a)–2(d). During all observed stages of the pattern evolution, an annular-shaped PS was visible, suggesting that a band of characteristic spatial frequencies was present in the patterns. Qualitatively, the radius of the annular region changed with increasing irradiation time, reflecting the change in morphology of the dewetting patterns. Figures 3(a)–3(d) show the pattern morphology after 100 pulses as a function of various energies for the 2 nm film. The general characteristics of the morphology were similar to those observed as a function of n, as shown in Fig. 2, and the primary role of increasing energy appears to be an enhanced rate of achieving the nanoparticle state.

2. Dewetting morphology for $3 \leq h \leq 7$ nm

For the thicker films, the intermediate stages of dewetting differed considerably in their morphology from Fig. 2 but still retained a characteristic spatial frequency. Figures 3(e)–3(h) capture the morphology of a 4.4-nm-thick Co film as a function of increasing number of laser pulses at energy of 93 mJ/cm^2. Discrete holes were visible after the shortest time [Fig. 3(e)], with the patterns changing to a cellular structure [Fig. 3(f)] as the number of holes increases. Continued irradiation results in the metal being pushed to the edge of the holes, and the patterns consisted of large polygonal structures with evidence for particle formation occurring preferentially at the vertices. This is more evident in Fig. 3(g). After long irradiation times, a stable nanostructure morphology was observed [Fig. 3(h)]. This behavior is consistent

with particle formation via capillary draining of the liquid bridges into the vertices (Sec. III B 3).

Analysis of the PS for each pattern again showed an annular structure, indicating spatial order in the dewetting patterns. The radial distribution function $g(k)$ obtained from the PS and the curve fit used to obtain L are shown in Fig. 4(a). The cumulative behavior of L vs n for this film is shown in Fig. 4(b). As in the case of the 2 nm film, L increases as the holes appear and merge to form closed ringlike polygons. In this scenario, L represents the average diameter of the holes or polygons. However, unlike the case of 2 nm film, the appearance of the nanoparticles decreases the characteristic length scale. This can be understood by noting that the final length scale represents the average NN spacing of the nanoparticles which formed preferentially at the vertices of the polygons. Since the average vertex spacing is smaller than the average diameter of the polygons, L therefore decreased as polygons changed into nanoparticles. The nanoparticles once again had a monomodal size distribution, as shown in Fig. 5(b). We also investigated the role of laser energy on the pattern formation. Similar to the case of the 2 nm film, we observed that the primary effect of increasing energy is an enhanced rate of achieving the nanoparticle state. This effect is better represented in Fig. 4(b), where the characteristic L determined from the $g(k)$ is plotted as a function of n for various laser energies E. As the laser energy increases, the observed value of L is larger, suggesting that the pattern ripening rate increased. However, R, which represented the nanoparticle morphology after long irradiation times, was independent of the laser E (Sec. III C). This result once again confirmed that the final nanoparticle state is robust to the laser parameters.
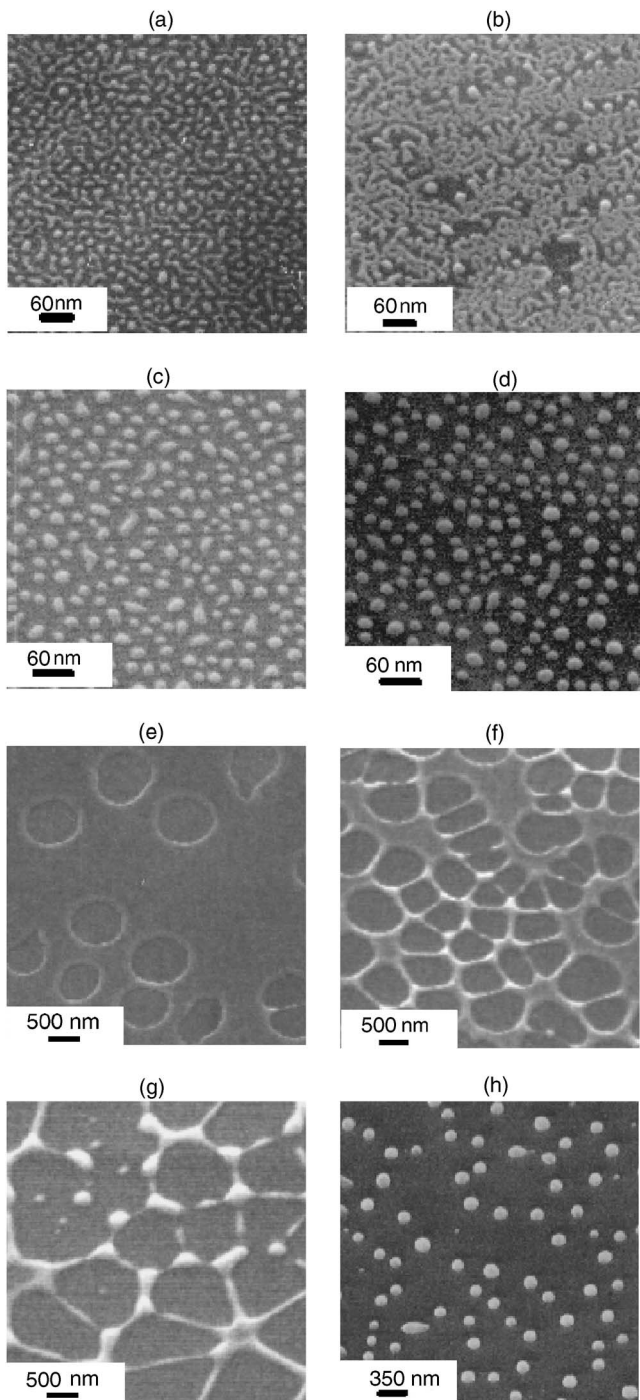
FIG. 3. SEM images of dewetting patterns in 2 nm Co film [(a)–(d)] irradiated as a function of laser energy density after 100 pulses and 4.4 nm Co film [(e)-(f)] irradiated at 93 mJ/cm² as a function of number of pulses n. (a) 190 mJ/cm² (b) 200 mJ/cm², (c) 220 mJ/cm², (d) 250 mJ/cm², (e) $n=10$, (f) $n=100$, (g) $n=1000$, and (h) $n=10\,500$.

3. Quantitative evidence for TFH instability

From the above results, we suggest that the pulsed-laser melting initiates the nonlinear dewetting TFH instability and subsequent pulses evolve this instability to a well-defined final state. Further, each observed state is characterized by a
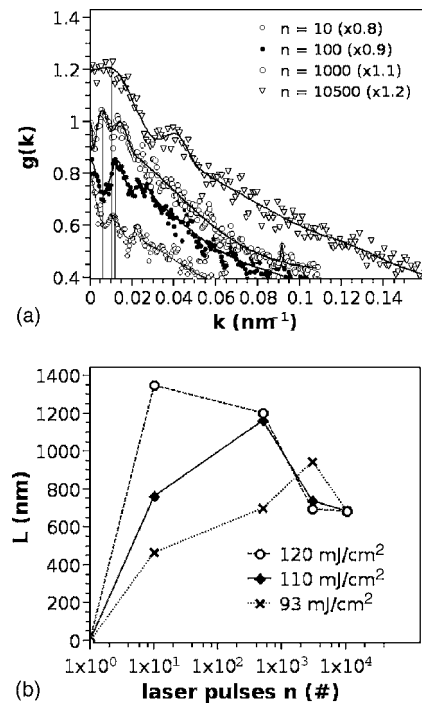
FIG. 4. Quantitative analysis of the spatial frequencies resulting from the short range order in the dewetting patterns for the 4.4 nm Co film. (a) The radial distribution function $g(k)$ for the patterns of Figs. 3(e)–3(h) showing an initial increase as the holes expand and then a decrease as the nanoparticles start to form. The vertical lines indicate peak positions in $g(k)$. (b) Behavior of the characteristic length extracted from the peak in $g(k)$ as a function of irradiation time n at various laser energies. The spacing of the final state is independent of the laser energy. The lines are guides for the eyes.

narrow band of spatial frequencies, indicating spatial order over the entire dewetting process. Since we ruled out heterogeneous nucleation from ordered surface defects, the above results point strongly to dewetting by an instability. A more quantitative evidence for this hypothesis can be pursued on the basis of predictions of the linear TFH theory, according to which the characteristic time scales and length scales of dewetting are well-defined functions of h. From our previous results, the most robust measure of the dewetting length scale appears to be the final nanoparticle state.[32] Therefore, we studied the characteristics of this final nanoparticle state including R, D, contact angle function $f(\theta)$, and the particle areal density N as a function of film thickness h to determine pattern formation via the TFH instability.

R vs h. According to the linear TFH instability, the characteristic spinodal length Λ as a function of film thickness can be expressed as:[15,17,19,32]

$$\Lambda(h) = \sqrt{\frac{16\pi^3\gamma}{A}}h^2 = Bh^2, \qquad (10)$$

where γ is the surface tension of the metal and A is the Hamaker constant. Since we interpret the final nanoparticle morphology as resulting from the dewetting instability, we assigned the observed NN spacing R to be proportional to Λ as $R=a\Lambda$, where a is the proportionality factor. This is rea-
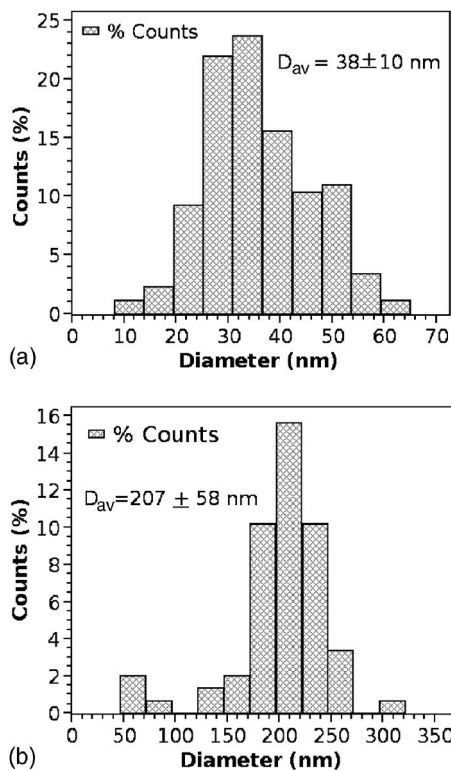
FIG. 5. Monomodal size distribution and average diameter of nanoparticles in the final robust state of laser-induced dewetting. (a) An average diameter of 38 nm results for the 2 nm Co film; (b) average diameter of 207 nm for the 4.4 nm Co film.
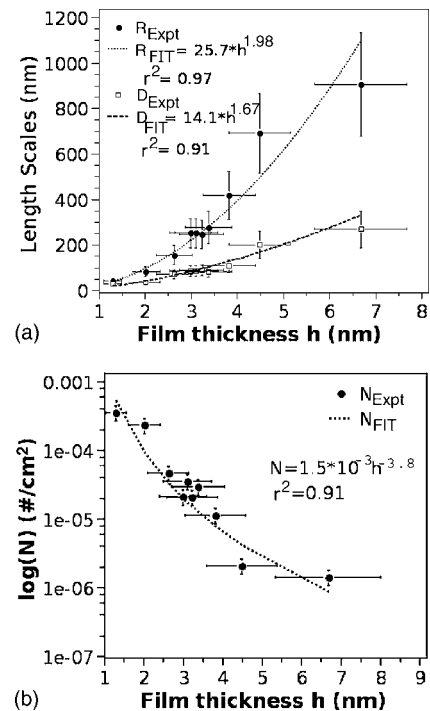

FIG. 6. Analysis of the various length scales in the final robust nanoparticle state as a function of film thickness. (a) The average nearest-neighbor spacing R of nanoparticles (closed circles) and the average nanoparticle diameter D (open squares), (b) The average areal density of nanoparticles N in nanoparticle/cm^2. The fits show exponents in good agreement with linear TFH theory. The r^2 values in each graph indicate the correlation coefficient of the least-squares fitting.

sonable given that the average nanoparticle spacing is related to the average size and/or spacing between the ordered features arising from the dewetting process. We determined the behavior of R as a function of film thickness, as shown by data represented by closed circles in Fig. 6(a). The power-law fit to the spacing R yielded a behavior expressed by $R(\text{nm}) = 25.7h^{1.98 \pm 0.3}$, with the film height expressed in nanometers. The NN spacings varied from ~40 to 1000 nm for the films studied. The exponent of the film thickness of 1.98 ± 0.3 is in good agreement to the theoretical value of 2. From this experimentally established preexponential factor of 25.7 nm^{-1}, the Hamaker constant was estimated to be $A = 1.41 \times 10^{-18}$ J, which is of the right order of magnitude.[46]

Dewetting instability time scale τ_D. In the multiple pulse laser melting dewetting scenario, the morphology change occurs over multiple cycles of phase change, i.e., melting and resolidification. Clearly, once the instability is initiated, in order for it to be fostered by the multiple pulses, the time scale of dewetting τ_D must be larger than the lifetime of the liquid τ_L in each pulse. From the linear TFH theory, τ_D can be expressed as

$$\tau_D(h) = \frac{96\pi^2 \gamma \eta}{A^2} h^5, \qquad (11)$$

where $\eta = 4.46 \times 10^{-3}$ Pa s is the viscosity of liquid Co at its melting point. Using the experimentally determined value of A, we find that $\tau_D \sim 25$ ns for a 1-nm-thick film and increases as h^5. From our modeling, we determined that at the

melt threshold of ~338 mJ/cm^2 for the 1 nm film, the liquid lifetime is ~4 ns. The typical liquid lifetime was obtained from thermal profiles of the type shown in Figs. 1(b) and 1(c). The liquid lifetime for the analytical result [Fig. 1(b)] was defined by placing a line at $T_m = 1768$ K, the Co melting temperature, and noting the time between both intercepts. For the numerical model [Fig. 1(c)], the liquid lifetime is defined as the time needed for the system to progress from the onset of melting to the completion of freezing. From this analysis, the liquid lifetime for the range of films studied here varied between 2 and 15 ns, as determined from the thermal model, and clearly is smaller than the dewetting time estimated from Eq. (11).

We also verified from the thermal modeling that the heating and cooling rates were extremely rapid, and since the time between pulses was large (20 ms), each pulse was thermally independent of the other. To extract the rates, first, plots of the type shown in Fig. 1(b) were generated for Co film thicknesses of 1, 2, 3, 5, and 11 nm, with laser energy density values chosen so that the peak temperature would be ~2000±100 K. The heating rate was estimated from the time Δt to reach maximum temperature T_m as $(T_m - T_0)/\Delta t$ and the model predicted typical rate of temperature rise of the bilayer system to be ~150 K/ns for the metal-film thicknesses of interest. For the cooling rates, and a second-order exponential fit to the cooling portion [e.g., Fig. 7(a)], a typical time constant of ~130 ns was estimated for the tempera-
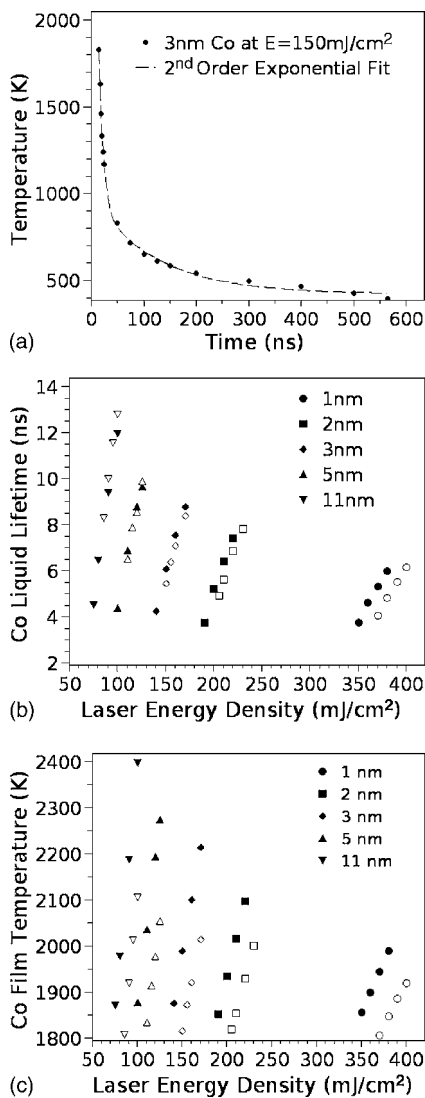
(a)

(b)

(c)

FIG. 7. (a) Analytical result of the cooling portion of thermal cycle for 3 nm Co on SiO_2 showing a fit using a second-order exponential function. Cumulative results of the analytical (closed symbols) and numerical models (open symbols) using T-dependent material parameters: (b) liquid lifetime vs laser energy density, and (c) peak temperature vs laser energy density. Closed symbols are analytical results, while the open symbols are from numerical calculations.

ture to fall by $1/e$ of its peak value. In addition, within approximately 500 ns, the bilayer system reached 98% of its final value giving a time-averaged cooling rate of ~4 K/ns. Clearly, each laser pulse could be treated independently of one another. These time scale estimates support a dewetting scenario, in which the instability is initiated by a number of pulses and then dewetting progresses by the subsequent pulses to the final stable nanoparticle state.

D and $f(\theta)$ vs h. An analytical relationship between the diameter of a particle D and the NN spacing R can be derived based on volume conservation.[20] Assuming that a circular section of the film with a volume approximated as a cylinder of diameter R and thickness h contributes to one spherical nanoparticle of diameter D, then volume conservation suggests that

$$\frac{\pi}{4}R^2h = \frac{4\pi}{3}f(\theta)\frac{D^3}{8},\qquad(12)$$

where $f(\theta)$ is the geometric factor based on the particle contact angle θ that determines the fraction of the sphere that lies above the substrate (for the case of $\theta=180°$, $f(\theta)=1$]. Using the characteristic length from Eq. (10) in Eq. (12), we get

$$D = \left[\frac{24\pi^3\gamma}{Af(\theta)}\right]^{1/3}h^{5/3} = Ch^{5/3}.\qquad(13)$$

In Fig. 6(a) (open squares), the average particle diameter D is plotted as a function of h. D varied from ~30 to 250 nm for the thickness range studied here. The power-law fit to our experimental data gives $D(nm)=14.8h^{1.6\pm0.3}$, with the film height expressed in nanometers. The exponent of 1.6 ± 0.3 is in good agreement with the theoretical estimate of $5/3$. By using the experimentally determined preexponent of 14.1 $nm^{-2/3}$ in Eq. (13), we determined the geometric factor to be $f(\theta)=0.361$, giving an effective contact angle for the nanoparticles of 74°. Given the simplicity of the model relating the instability of length scale to the particle diameter and the uncertainties in the values of R and D of approximately 30%, this experimentally extracted value of the contact angle is in reasonable agreement to the previously reported value of $100\pm26°$ measured by atomic force and scanning electron microscopies.[33]

Areal density N vs h. The areal density N of particles can be defined as

$$N = 1/\left(\frac{\pi}{4}\Lambda^2\right),\qquad(14)$$

which, using Eq. (10), results in a thickness dependence given by

$$N(h) = \frac{A}{4\pi^4\gamma}h^{-4}.\qquad(15)$$

Plotted in Fig. 6(b) is the variation in the observed particle density with h. A power-law fit gives $N=1.5\times10^{-3}h^{-3.8\pm0.8}$ nanoparticle/nm^2, with the film height expressed in nanometers. The exponent of -3.8 ± 0.8 is in good agreement with the expected value of 4 (with the uncertainty primarily arising from propagating errors in the various quantities), while the preexponent is consistent with the value obtained by substituting the experimentally determined A and γ in Eq. (15).

Effect of large capillary velocity on pattern formation. From the quantitative results above, the classical TFH dewetting instability appears to be a suitable explanation for the pattern formation in these nanoscopic Co films in the regime of weak thermocapillary effects. At this stage, it is also important to emphasize the difference between the dewetting patterning behavior observed in the metal films reported here to those of typical polymer films.[20] Previous studies of the breakup of cellular structures made from typical polymeric liquids show that the sides of the polygons break into a chain of droplets by the Rayleigh instability and, as a consequence, the particle diameter will follow the trend $D\sim h^{3/2}$.[20] How-

ever, for the metal films investigated here, the final breakup of the cellular regions most likely occurs via capillary flow of the liquid into the vertices of the polygon. We arrived at this conclusion based on the close correlation in the spatial density of the vertices and particles [Figs. 3(g) and 3(h)] or the spaghettilike features and particles in Figs. 2(c) and 2(d). We attribute this to the extremely large capillary velocities[47,48] of the liquid metals given by the quantity $v_c = \gamma/\eta$, which for Co is ~422 m/s. This implies that capillary draining from the liquid bridges connecting the vertices (reservoirs) which are separated by a distance of 1 μm (which is smaller than the largest NN spacing reported in this work) is ~2.5 ns. This is smaller than the (Rayleigh) ripening time $[\tau_{Ray} \sim 2\pi(\rho r^3/c\gamma)^{1/2}]$, where ρ is the liquid density, r is the cylinder radius, and c is a factor of $O(0.1)$ determined by contact angle and boundary conditions, for surface perturbations of the liquid bridges, which typically ranged between several to >10 ns for the bridge sizes observed here.[49] In this respect, the final stages of breakup are different from that typically observed in common polymer films investigated, such as polystyrene, in which the cellular rims break up via a Rayleigh-like instability.[20] Moreover, we point out that the Ohnsorge number, $Oh \equiv \frac{\eta}{\sqrt{\rho\gamma D}}$, that represents the ratio of viscous to capillary forces is typically ≪1 for typical $O(10$ nm) values of the liquid bridge diameter D. This further underscores the dominance of strong capillary effects in the breakup of polygonal structures. For more viscous liquids (e.g., polymers) with typically smaller interfacial tension as compared to metals, the relative importance of viscous and capillary forces can change by orders of magnitude, leading to different mechanisms of breakup, e.g., via Rayleigh-like process. Another factor that can influence the particle size distribution is coarsening due to surface diffusion. However, as seen from Fig. 4(b), changing the laser energy, which changes liquid temperature and lifetime (Sec. III C), did not change the final spacing. This was attributed to the fast thermal processing that minimizes particle coarsening.

C. Role of Co liquid temperature and lifetime on dewetting

From the experimental results of dewetting presented in the previous section, the length scales L during the early stages of dewetting increased with increasing laser energy following similar irradiation times (Fig. 4). From our thermal modeling, increasing laser energy increased the Co liquid temperature and the liquid lifetime. Further, the length scale of dewetting Λ and the dewetting time scale τ_D have temperature-dependent material parameters (i.e., γ and η). Therefore the observations of Fig. 4 can arise from three factors: (i) from a change in the dewetting length scale Λ, (ii) from an increase in liquid lifetime τ_L per pulse, and (iii) from a change in the time scale for ripening τ_R of the dewetting structures. However, Fig. 4 also indicates that changing the laser energy had no influence on the final nanoparticle characteristic, implying that no permanent change to Λ must occur with change in liquid T_L. In this section, we show that the change in Λ for Co metal is experimentally indistinguishable over significant T changes (of up to 500 K above T_m). From theoretical arguments, we found that the increase in L with

increasing E following irradiation by a small number of pulses n (i.e., early stages) arises primarily due to variations in τ_L and its linear behavior with E. This result was also consistent with experimental observations based on the measurement of L vs n for various energies and thicknesses.

1. Role of temperature on Λ

The T dependence of the dewetting length Λ, which comes from the surface tension $\gamma(T)$ and the Hamaker constant $A(T)$, can be expressed as

$$\Lambda(h,T) = \sqrt{\frac{16\pi^3\gamma(T)}{A(T)}}h^2. \tag{16}$$

The variation in temperature can be expressed as

$$\frac{d\Lambda}{dT} = \sqrt{16\pi^3}\left[\frac{1}{2A^{1/2}}\gamma^{-1/2}\frac{\partial\gamma}{\partial T} - \frac{\gamma^{1/2}}{2A^{3/2}}\frac{\partial A}{\partial T}\right]h^2. \tag{17}$$

Equation (17) can be simplified for metals on SiO_2 system by noting that the Hamaker constant for metals is virtually independent of temperature[50] and so $\frac{\partial A}{\partial T} \sim 0$ resulting in

$$\frac{d\Lambda}{dT} = \sqrt{16\pi^3}\left[\frac{1}{2A^{1/2}}\gamma^{-1/2}\frac{\partial\gamma}{\partial T}\right]h^2. \tag{18}$$

For a temperature rise of ΔT over the melting point, the change in length can be expressed as

$$\Delta\Lambda(\Delta T) = \frac{\Lambda(T_m)}{2\gamma(T_m)}\frac{d\gamma}{dT}\Delta T = -2.66\times10^{-4}\Lambda(T_m)\Delta T, \tag{19}$$

where $\Lambda(T_m)$ is the length at the melt temperature, and $\gamma(T_m)$ and $d\gamma/dT$ for Co are taken from Table I. From this, we see that Λ decreases as T_L increases, but this decrease is small and for temperature rises of up to $\Delta T = 500$ K is only ~−13%. This change is smaller than the spread in the experimental values of R of ±20% as measured from the $g(k)$. Therefore, for conditions under which the Co liquid T rise is ~500 K above T_m, the change in length scale will be experimentally indistinguishable.

2. Role of T on ripening rate L/n

According to the linear TFH theory, the pattern ripening time τ_R is expected to be proportional to the dewetting time τ_D,[15] and so we can express the T-dependent ripening time as

$$\tau_R(h,T) = \omega\tau_D = \omega\frac{96\pi^3\gamma(T)\eta(T)}{A(T)^2}h^5. \tag{20}$$

From this we can also define the ripening rate as $\sigma \propto \frac{\Lambda}{\tau_R}$, which can be evaluated using Eqs. (16) and (20) as

$$\sigma(h,T) = \kappa\frac{\Lambda(h,T)}{\tau_R(h,T)} = M\gamma(T)^{-1/2}\eta(T)^{-1}A^{1/2}h^{-3}, \tag{21}$$

where $M = \frac{\kappa}{\omega}\frac{\sqrt{16\pi^3}}{96\pi^3}$ is a proportionality constant with unknown numerical factors of κ and ω. Using these expressions, the experimentally observed dewetting length L for a film of
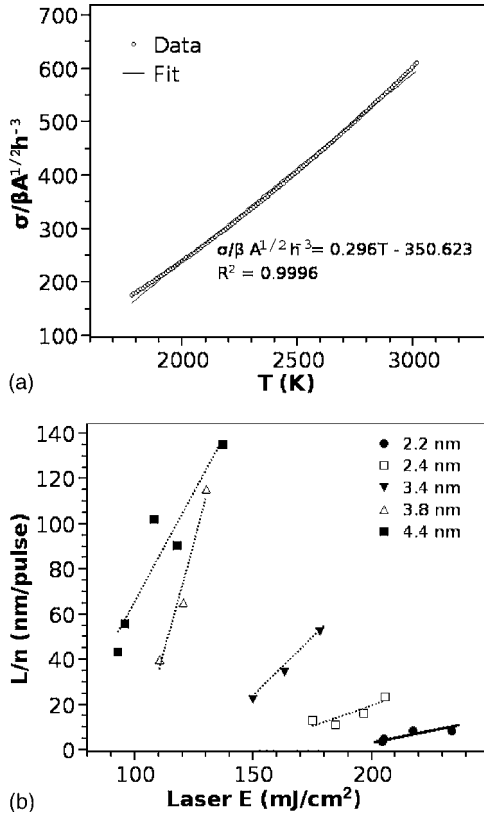
FIG. 8. Role of temperature on the ripening rate of dewetting. (a) A linear dependence of the spinodal ripening rate is predicted from the temperature dependence of the Co liquid material parameters (Table I). (b) The experimentally observed ripening rate L/n for various film thicknesses and energies. The symbols are experimental data, while the lines are linear fits.

thickness h at a given laser energy $E > E_m$ following irradiation by n pulses can be expressed as

$$L(h,E,n) = \sigma(h,E)\tau_L(E,h)n, \qquad (22)$$

where τ_L, the lifetime of the liquid, is a function of the laser energy and film thickness. In order to evaluate the expected behavior, each of the temperature-dependent (and laser E) terms on the right-hand side can be evaluated.

Behavior of ripening rate $\sigma(h,T)$ for Co. The temperature dependence of σ can be expressed analytically as

$$\frac{d\sigma(T,h)}{dT} = -B\frac{A^{1/2}}{\gamma^{1/2}\eta}h^{-3}\left[\frac{1}{2}\frac{\gamma_T}{\gamma} + \frac{\eta_T}{\eta}\right], \qquad (23)$$

where $\gamma_T = \frac{\partial\gamma}{\partial T}$ and $\eta_T = \frac{\partial\eta}{\partial T}$, and the temperature dependence of the Hamaker constant has been neglected. The behavior of $\sigma(T)$ with temperature can be evaluated for Co metal by using the material parameters from Table I. Figure 8(a) shows that Eq. (23) is well described by a linear behavior, which increases with increasing temperature, of the form

$$\sigma(T,h) = \beta A^{1/2}h^{-3}[0.29T - 350] = \sigma_T(h)T - \sigma_o(h). \qquad (24)$$

Dependence on liquid T and lifetime τ_L on E: Thermal modeling. From thermal profiles of the type shown in Fig. 1(a), the peak temperature and liquid lifetime were calculated as functions of h and E. Figure 1(b) shows thermal profiles of the film temperature for various film thicknesses for a laser energy density value of $E = 125$ mJ/cm². The liquid lifetime for the analytical model was defined by placing a line at $T_m = 1768$ K, the Co melting temperature, and noting the time in between both intercepts. For the numerical model, the liquid lifetime is defined as the time needed for the system to progress from the onset of melting to the completion of freezing. From Fig. 1(b), we see that introducing phase change into the model causes an appreciable change from the predicted temporal profile by Eq. (8). The portions of the figure where the temperature plateaus represent the film melting and freezing. Figure 7(b) presents the liquid lifetime and peak temperature versus laser energy density trends using the numerical and analytical models. From the figure, the numerical (open symbols) predictions for liquid lifetimes are about 20% lower than those predicted by the analytical model (closed symbols) for films greater than 1 nm. Further, from Fig. 7(c), the peak temperatures predicted by the numerical simulation are lower by ~ 200 K than those predicted by the analytical model. Both these differences arise from the fact that the phase change in the numerical model consumes more energy and takes more time. Figures 7(b) and 7(c) present the liquid lifetime and peak temperature as a function of laser energy density above the melt threshold for various film thicknesses. From thermal cycles of the type shown in Fig. 1, a linear relationship was observed between the liquid lifetime and peak temperature for small changes in laser energy density above E_m and can be expressed as

$$\tau_L(E,h) = A(h)E - B(h), \qquad (25)$$

$$T_L(E,h) = C(h)E + D(h), \qquad (26)$$

where the slopes A and C and intercepts B and D are thickness-dependent positive quantities. Their typical values are in the range $0.07 \leq A \leq 0.3$ ns cm²/mJ, $-22 \leq B \leq -17$ ns, and $2.3 \leq C \leq 14.5$ K cm²/mJ; and $D \sim 301$ K for thickness in the range $1 \leq h \leq 11$ nm, with less than 5% difference between the numerical and analytical estimates. In this laser energy density regime, while the temperature of the Co film is above the melting temperature, there is minimal evaporation over the relevant time scales.

Using Eq. (25) in Eq. (22) and Eq. (26) in Eq. (24), we can express the rate of change of dewetting length L with n as

$$\frac{L(E,h)}{n} = pE^2 + qE + r, \qquad (27)$$

where $p = \sigma_T CA$, $q = \sigma_T(DA - BC) - \sigma_o A$, and $r = -B(\sigma_T D - \sigma_o)$ are the resulting temperature and thickness coefficients. Equation (27) can be further simplified by analyzing the magnitudes of the various coefficients using the range of values for the coefficients $A-D$, which showed that for films in the range of $1-11$ nm at the melting point of Co, the

coefficient $p \ll q$ and the quadratic term in Eq. (27) can be neglected to give

$$\frac{L(E,h)}{n} = qE + r. \tag{28}$$

Therefore the experimentally observed trend in the ripening rate with laser energy should be linear. As shown in Fig. 8(b), the L/n for for various film thicknesses can be described by linear fits (dashed lines). The physical significance of this linear behavior is the weak temperature dependence of the material parameters of Co. Therefore the primary contribution to the ripening rate due to increasing energy is the increasing lifetime of the liquid, which, as shown in Fig. 7(b), varies linearly with E. This result also implied that understanding the thermal behavior could result in predictive models describing the quenched-in dewetting morphologies and length scales when such nanoscopic films are subjected to multiple instances of phase change.

IV. SUMMARY AND CONCLUSIONS

We have investigated the dewetting behavior of nanoscopic Co metal films with thickness $h < \alpha_m^{-1}$ on SiO$_2$ substrates following multiple nanosecond pulse laser irradiation using 266 nm UV light through experiments, first-principles thermal transport modeling, and analysis based on TFH theory. We determined that by accounting appropriately for the changes with respect to h in the reflectivity of the substrate-metal bilayer, quantitative agreement with experiments can be obtained for the h dependence of the melting energy threshold predicted by *continuum-level* analysis. This observation corroborates atomistic simulations of heat transport for simpler systems under shear flow, where the results were found to agree with the predictions of continuum-level analysis for liquid layers with several atomic layers. For the metal films used in this work, this translates to $h < 1$ nm. A different effect, the development of intrinsic thermal gradients $\partial T / \partial h$ whose sign is positive for h less than a critical value $h_c \approx 9-13$ nm and negative for $h > h_c$, was predicted by the thermal model. This effect arises due to the strong film thickness and time dependences of temperature for liquid metal nanolayers and fast thermal cycles. This intrinsic effect can lead to thermocapillary effects that could modify pattern formation. However, for the experimental thickness regime investigated, the thermal diffusion time scales τ_H is less than or equal to the pulse time $t_p = 9$ ns and therefore the influence of $\partial T / \partial h$ is minimal. However since $\tau_H \propto h^4$, thermocapillary mechanisms could be important for thicker films, a hypothesis that needs to be verified by future experimental studies. Because of the extremely fast thermal cycles [heating and/or cooling rates of $O(10^{10}$ K/s)] and short liquid lifetimes τ_L of $2-15$ ns, multiple pulses were required to observe the thin-film instability with characteristic dewetting times $\tau_D \gtrsim 25$ ns. The dewetting patterns showed short-range order and typically evolved with increasing number of laser pulses from discrete holes to bicontinuous or cellular structures and eventually into nanoparticles. The large capillary velocity and short patterning length scales in the metal layer resulted in nanoparticle formation by capillary flow rather than via a Rayleigh-like breakup typically observed in polymer liquids. This behavior can be attributed to the unique thermophysical properties of the metals, including the large γ, small η, and large Hamaker constant A that result in large capillary velocities and small patterning length scales. This final nanoparticle state was extremely robust with nearest-neighbor spacing $R \sim h^2$ and a monomodal size distribution with diameter $D \sim h^{5/3}$, respectively. This robustness was due to the relatively weak temperature dependence of the thermophysical parameters of Co and small particle ripening rates due to the fast thermal processing. The experimental ripening rate L/n increased linearly with laser energy density E at the early stages of patterning and due to the linear increase in τ_L liquid lifetime with E predicted by the thermal modeling, implying that accurate predictions and control of the quenched-in dewetting morphologies and length scales can be achieved in these nanoscopic systems. These results show that nanoscopic metal-film dewetting following fast thermal processing results in different quenched-in dewetting morphologies and length scales which can be accurately predicted by first-principles modeling.

*Electronic address: suresh@che.wustl.edu

†Electronic address: ramkik@wuphys.wustl.edu

[1] S. Sun, C. Murray, D. Weller, L. Folks, and A. Moser, Science **287**, 1989 (2000).

[2] S. Fan, M. Chapline, N. Franklin, T. Tombler, A. Cassell, and H. Dai, Science **283**, 512 (1999).

[3] S. Maier, P. Kik, H. Atwater, S. Meltzer, E. Harel, B. Koel, and A. Requicha, Nat. Mater. **2**, 229 (2003).

[4] S. A. Maier, P. G. Kik, and H. A. Atwater, Phys. Rev. B **67**, 205402 (2003).

[5] M. Quinten, A. Leitner, J. Krenn, and F. Aussenegg, Opt. Lett. **23**, 1331 (1998).

[6] R. White, J. Magn. Magn. Mater. **209**, 1 (2000).

[7] H. Garcia, J. Trice, R. Kalyanaraman, and R. Sureshkumar, Phys. Rev. B **75**, 045439 (2007).

[8] P. Sigmund, J. Mater. Sci. **8**, 1545 (1965).

[9] R. Bradley and J. Harper, J. Vac. Sci. Technol. A **6**, 2390 (1988).

[10] E. Chason, T. M. Mayer, B. K. Kellerman, D. T. McIlroy, and A. J. Howard, Phys. Rev. Lett. **72**, 3040 (1994).

[11] J. Erlebacher, M. J. Aziz, E. Chason, M. B. Sinclair, and J. A.

Floro, Phys. Rev. Lett. **82**, 2330 (1999).

[12] S. Facsko, T. Dekorsy, and H. Kurz, Phys. Rev. B **63**, 165329 (2001).

[13] R. Moroni, D. Sekiba, F. Buatier de Mongeot, G. Gonella, C. Boragno, L. Mattera, and U. Valbusa, Phys. Rev. Lett. **91**, 167207 (2003).

[14] M. Xu and C. Teichert, J. Appl. Phys. **96**, 2244 (2004).

[15] A. Vrij, Discuss. Faraday Soc. **42**, 23 (1966).

[16] A. Sharma and E. Ruckenstein, Langmuir **2**, 480 (1986).

[17] A. Sharma, Langmuir **9**, 861 (1993).

[18] R. Seemann, S. Herminghaus, and K. Jacobs, Phys. Rev. Lett. **86**, 5534 (2001).

[19] F. Brochard Wyart and J. Daillant, Can. J. Phys. **68**, 1084 (1990).

[20] G. Reiter, Phys. Rev. Lett. **68**, 75 (1992).

[21] U. Thiele, M. Mertig, and W. Pompe, Phys. Rev. Lett. **80**, 2869 (1998).

[22] T. Stange and D. Evans, Langmuir **13**, 4459 (1997).

[23] U. Thiele, M. G. Velarde, and K. Neuffer, Phys. Rev. Lett. **87**, 016104 (2001).

[24] R. Pretorius, J. Harris, and M. Nicolet, Solid-State Electron. **21**, 667 (1978).

[25] L. H. Ho, T. Nguyen, J. C. Chang, B. Machesney, and P. Geiss, J. Mater. Res. **8**, 467 (1993).

[26] X. Hu, D. Cahill, and R. Averback, Appl. Phys. Lett. **76**, 3215 (2000).

[27] X. Hu, D. G. Cahill, and R. S. Averback, J. Appl. Phys. **89**, 7777 (2001).

[28] C. Favazza, J. Trice, H. Krishna, and R. Kalyanaraman, *Surface Engineering for Manufacturer Applications*, MRS Symposia Proceedings No. 890 (Materials Research Society, Pittsburgh, 2006), pp. 0890-Y04-06.1-06.6.

[29] S. J. Henley, J. D. Carey, and S. R. P. Silva, Phys. Rev. B **72**, 195408 (2005).

[30] J. Bischof, M. Reinmuth, J. Boneberg, S. Herminghaus, T. Palberg, and P. Leiderer, Proc. SPIE **2777**, 119 (1996).

[31] S. Herminghaus, K. Jacobs, K. Mecke, J. Bischof, A. Fery, M. Ibn-Elhaj, and S. Schlagowski, Science **282**, 916 (1998).

[32] C. Favazza, R. Kalyanaraman, and R. Sureshkumar, Nanotechnology **17**, 4229 (2006).

[33] C. Favazza, J. Trice, H. Krishna, R. Kalyanaraman, and R. Sureshkumar, Appl. Phys. Lett. **88**, 153118 (2006).

[34] C. Favazza, J. Trice, A. Gangopadhyay, H. Garcia, R. Sureshkumar, and R. Kalyanaraman, J. Electron. Mater. **35**, 1618 (2006).

[35] R. Khare, J. de Pablo, and A. Yethiraj, J. Chem. Phys. **107**, 2589 (1997).

[36] C. Zhang and R. Kalyanaraman, Appl. Phys. Lett. **83**, 4827 (2003).

[37] W. Zhang, C. Zhang, and R. Kalyanaraman, J. Vac. Sci. Technol. B **23**, L5 (2005).

[38] E. Matthias, M. Reichling, J. Siegel, O. W. Kading, S. Petzoldt, H. Skurk, P. Bizenberger, and E. Neske, Appl. Phys. A: Solids Surf. **58**, 129 (1994).

[39] B. Yilbas and S. Shuja, J. Phys. D **32**, 1947 (1999).

[40] N. Semmar and C. Boulmer-Leborgne, J. Phys. IV **120**, 413 (2004).

[41] O. S. Heavens, *Optical Properties of Thin Solid Films* (Butterworth, London, 1955), pp. 76–77.

[42] V. Voller and C. Prakash, Int. J. Heat Mass Transfer **30**, 1709 (1987).

[43] R. Lewis, P. Nithiarasu, and K. Seetharamu, *Fundamentals of the Finite Element Method for Heat and Fluid Flow* (Wiley, West Sussex, 2004).

[44] J. H. Weaver, C. Krafka, D. W. Lunch, and E. E. Koch, *Physics Data, Optical Properties of Metals* (Fachinformationszentrum Energie, Physik, Matematik GmbH, Karlsuhe, 1981), Vol. 18.

[45] P.-G. de Gennes, F. Brochard-Wyart, and D. Quere, *Capillarity and Wetting Phenomenon* (Springer, New York, 2003).

[46] J. Israelachvili, *Intermolecular and Surface Forces* (Academic, London, 1992).

[47] J. Eggers, J. Lister, and H. Stone, J. Fluid Mech. **401**, 293 (1999).

[48] D. G. A. L. Aarts, M. Schmidt, and H. N. W. Lekkerkerker, Science **304**, 847 (2004).

[49] Y. Amarouchene, D. Bonn, J. Meunier, and H. Kellay, Phys. Rev. Lett. **86**, 3558 (2001).

[50] R. French, J. Am. Ceram. Soc. **83**, 2117 (2000).

[51] *The CRC Handbook of Chemistry and Physics*, edited by D. Linde (CRC, Boca Raton, FL, 1992).

[52] N. Bansal and R. Doremus, *Handbook of Glass Properties* (Academic, Orlando, FL, 1986).

[53] R. Tyagi and R. Mathur, J. Phys. D **3**, 1811 (1970).

[54] S. Montague, C. Draper, and G. Rosenblatt, J. Phys. Chem. Solids **40**, 987 (1979).